Direct numerical simulation and Reynolds-averaged Navier-Stokes modeling of the sudden viscous dissipation for multicomponent turbulence

Alejandro Campos and Brandon E. Morgan

Phys. Rev. E **99**, 063103 — Published 5 June 2019
DOI: 10.1103/PhysRevE.99.063103

Direct numerical simulation and Reynolds-averaged Navier-Stokes modeling of the sudden viscous dissipation for multicomponent turbulence

Alejandro Campos* and Brandon E. Morgan
Lawrence Livermore National Laboratory, Livermore, California 94550, USA
(Dated:)

Simulations of a turbulent multicomponent fluid mixture undergoing isotropic deformations are carried out to investigate the sudden viscous dissipation. This dissipative mechanism was originally demonstrated using simulations of an incompressible single-component fluid [Davidovits and Fisch, Phys. Rev. Lett. 116, 105004(2016)]. By accounting for the convective and diffusive transfer of various species, the current work aims to increase the physical fidelity of previous simulations and their relevance to inertial confinement fusion applications. Direct numerical simulations of the compressed fluid show that the sudden viscous dissipation of turbulent kinetic energy is unchanged from the single-component scenario. More importantly, the simulations demonstrate that the mass fraction variance and covariance for the various species also exhibit a sudden viscous decay. Reynolds-averaged Navier-Stokes simulations were carried out using the *k*-*l* model to assess its ability to reproduce the sudden viscous dissipation. Results show that the standard *k*-*l* formulation does not capture the sudden decay of turbulent kinetic energy, mass-fraction variance, and mass-fraction covariance for simulations with various compression and expansion rates, or different exponents for the power-law model of viscosity. A new formulation of the *k*-*l* model that is based on previous improvements to the *k*-ϵ family of models is proposed, which leads to consistently good agreement with the direct numerical simulations for all the isotropic deformations under consideration.

I. INTRODUCTION

Numerical simulations were used by Ref. [1] to demonstrate that the isotropic compression of a turbulent flow field leads to a rapid and sudden viscous dissipation of turbulent kinetic energy (TKE). The dissipated TKE is transformed into heat, which can then be used to enhance ignition conditions in either laser-driven or Z-pinch-driven inertial confinement fusion (ICF). This sudden viscous dissipative mechanism occurs for substances whose viscosity has a strong scaling on temperature, as is the case for some plasmas ($\mu \sim T^{5/2}$ [2]) rather than traditional fluids ($\mu \sim T^{3/4}$ [3]).

The original simulations of Ref. [1] relied on a simplified formulation in which the plasma is treated as an incompressible fluid with a temperature-dependent power law for the viscosity and a fixed time history for the temperature. Subsequent work has focused on increasing the fidelity of these simulations. For example, Ref. [4] modifies the viscosity power law by accounting for the ionization state Z of the plasma. Expressing the viscosity as $\mu \sim T^n/Z^m \sim T^\beta$, where β depends on the the model used for the plasma charge state, it was shown that the sudden viscous dissipation occurs for $\beta > 1$ only. Additionally, Ref. [5] simulated the compression of an imploding spherical turbulence layer, rather than a homogeneous turbulent flow. The sudden viscous dissipation was shown to occur for this new scenario as well. Finally, Ref. [6] relaxes the assumption of low-Mach number turbulence, and accounts for finite Mach number effects in the sudden viscous dissipation of TKE. Results indicate that for subsonic turbulent Mach numbers, the available energy in the turbulent fluctuations is not sufficient to significantly alter the temperature evolution of the fluid.

As stated in Ref. [6], although previous research on the sudden viscous dissipation has increasingly included more relevant physics, simulations carried out so far are not yet truly representative of ICF scenarios, which are characterized by additional physical phenomena such as mass transfer, radiative heat transfer, complex equations of state, and multicomponent plasma viscosity models, among others. The aim of the current study is thus to further increase the fidelity of simulations used to predict the sudden viscous dissipation by accounting for the convective and diffusive mass transfer in a multicomponent fluid. Given that mixing of various components in ICF degrades capsule performance [7], multicomponent simulations should eventually be used to account for the detrimental effect of turbulent mixing when assessing the favorable effect of the sudden viscous dissipation. Additionally, a multicomponent formulation paves the way forward for simulations that account for multicomponent plasma viscosities

* campos33@llnl.gov

models [8] and nuclear reactions.

In this paper, results from Direct Numerical Simulations (DNS) are reported to determine differences between the TKE evolution of a five-component mixture and that of a single-component fluid. Of even more interest, however, is the evolution of the mass-fraction variance and covariance for the various species, since the species diffusivity, which behaves similarly to the fluid viscosity, can also lead to sudden dissipative phenomena. It is important to accurately predict the mass-fraction variance and covariance since these quantities are used as inputs to reaction-rate models [9]. In addition to direct numerical simulations, the current work focuses on the formulation of an improved Reynolds-averaged Navier-Stokes (RANS) model to capture the sudden viscous dissipation. This proposed new model is based on the variable-density k-l family of closures that are commonly used to simulate phenomena of relevance to ICF, such as buoyancy-, shock-, and shear-driven instabilities [10]. Thus, by using traditional k-l models to improve the prediction of the sudden viscous dissipation, it is hoped that the final formulation will have a broader range of applicability than models tailored specifically to capture the sudden viscous dissipation of TKE, such as that proposed in [11]. Predictions obtained with the original and modified RANS models are compared against DNS results for the isotropic compressions, as well as DNS results for an isotropic expansion, so as to again ensure a broad range of applicability.

The outline of the paper is as follows. Section II describes the direct numerical simulations of the multicomponent fluid mixture. This section includes the governing equations in Sec. II A, transformed equations suitable for computational simulations in Sec. II B, details of the numerical framework in Sec. II C, a description of the initial conditions in Sec. II D, and profiles for the TKE, mass-fraction variance, and mass-fraction covariance in Sec. II E. The RANS framework is the focus of Sec. III. The Reynolds-averaged governing equations for homogeneous multicomponent turbulence undergoing isotropic mean-flow deformations are given in Sec. III A, the derivation of the new formulation of the k-l model is given in Sec. III B, and results for the TKE, mass-fraction variance, and mass-fraction covariance obtained with the original and modified k-l models are given in Sec. III C. Finally, the paper ends with conclusions and a discussion of future work in Sec. IV.

II. DIRECT NUMERICAL SIMULATIONS

A. Multicomponent Navier-Stokes equations

The governing equations for the direct numerical simulations are the multicomponent Navier-Stokes equations. The transport partial differential equations for the density ρ, velocity u_i, total energy E, and species mass fraction Y_α are

$$\frac{\partial \rho}{\partial t} + \frac{\partial \rho u_i}{\partial x_i} = 0, \tag{1}$$

$$\frac{\partial \rho u_i}{\partial t} + \frac{\partial \rho u_i u_j}{\partial x_j} = -\frac{\partial p}{\partial x_i} + \frac{\partial t_{ij}}{\partial x_j}, \tag{2}$$

$$\frac{\partial \rho E}{\partial t} + \frac{\partial}{\partial x_i}\left[\rho\left(E + \frac{p}{\rho}\right)u_i\right] = \frac{\partial u_i t_{ij}}{\partial x_j} - \frac{\partial q_i}{\partial x_i}, \tag{3}$$

$$\frac{\partial \rho Y_\alpha}{\partial t} + \frac{\partial \rho Y_\alpha u_i}{\partial x_i} = -\frac{\partial J_{\alpha,i}}{\partial x_i}. \tag{4}$$

In the above, the pressure is denoted by p. The shear-stress tensor t_{ij}, the heat flux q_i, and the diffusive flux $J_{\alpha,i}$ of each species α are

$$t_{ij} = 2\mu S_{ij} + \left(\beta - \frac{2}{3}\mu\right)\frac{\partial u_k}{\partial x_k}\delta_{ij}, \tag{5}$$

$$q_i = -\kappa \frac{\partial T}{\partial x_i} + \sum_\alpha h_\alpha J_{\alpha,i}, \tag{6}$$

$$J_{\alpha,i} = -\rho D \frac{\partial Y_\alpha}{\partial x_i}. \tag{7}$$

S_{ij} is the rate-of-strain tensor, T the temperature, and h_α the enthalpy of species α. Four transport coefficients appear in the equations above, namely the dynamic viscosity μ, the bulk viscosity β, the thermal conductivity κ, and the diffusivity D. The diffusivity is assumed to be equal for all species. Expressions for the transport coefficients are

$$\mu = \mu_0 \left(\frac{T}{T_0}\right)^n, \tag{8}$$

$$\beta = 0, \tag{9}$$

$$\kappa = \frac{\mu C_p}{\mathrm{Pr}}, \tag{10}$$

$$D = \frac{\mu}{\rho \mathrm{Sc}}. \tag{11}$$

μ_0 and T_0 are the reference viscosity and temperature, respectively, n is the power-law exponent, C_p the specific heat at constant pressure, Pr the Prandtl number, and Sc the Schmidt number. Each species is treated as an ideal gas, and thus the following relationships hold

$$p_\alpha = \rho_\alpha R_\alpha T, \tag{12}$$

$$R_\alpha = \frac{R_u}{M_\alpha}, \tag{13}$$

$$e_\alpha = C_{v,\alpha} T, \tag{14}$$

$$h_\alpha = C_{p,\alpha} T. \tag{15}$$

p_α is the species pressure, ρ_α the species density, R_u the universal gas constant, M_α the species molar mass, e_α the species internal energy, $C_{v,\alpha}$ the species specific heat at constant volume, and $C_{p,\alpha}$ the species specific heat at constant pressure. The mixture properties are obtained from the species variables using

$$e = \sum_\alpha Y_\alpha e_\alpha \qquad C_v = \sum_\alpha Y_\alpha C_{v,\alpha}, \tag{16}$$

$$h = \sum_\alpha Y_\alpha h_\alpha \qquad C_p = \sum_\alpha Y_\alpha C_{p,\alpha}, \tag{17}$$

$$p = \sum_\alpha V_\alpha p_\alpha \qquad V_\alpha = \frac{\rho Y_\alpha}{\rho_\alpha}, \tag{18}$$

where e, h, and C_v are, respectively, the internal energy, the enthalpy, and the specific heat at constant volume, for the entire mixture. V_α is the volume fraction of species α. Finally, the following equations are required to complete the system

$$E = e + K, \tag{19}$$

$$K = \frac{1}{2} u_i u_i, \tag{20}$$

$$S_{ij} = \frac{1}{2}\left(\frac{\partial u_i}{\partial x_j} + \frac{\partial u_j}{\partial x_i}\right). \tag{21}$$

B. Transformed multicomponent Navier-Stokes equations

Rather than solving the equations described in the previous section, one can extend the derivations of Ref. [1] for incompressible single-species flow, or the derivations in Ref. [6] for compressible single-species flow, so as to obtain the corresponding transformed equations for a compressible multi-species mixture. This new set of equations are formulated with respect to a moving reference frame that shrinks as the flow is compressed, or grows as the flow is expanded. Thus, these set of equations are preferred for direct numerical simulations since they allow for a fixed grid with periodic boundary conditions. The resulting equations are identical to those in Sec. II A, except that the total velocity u_i is replaced by the Favre-fluctuating velocity u_i''. This fluctuating velocity is defined as $u_i'' = u_i - \widetilde{u}_i$, where $\widetilde{u}_i$ is the Favre-averaged velocity. In addition, each of Eqs. (1) to (4) is augmented with forcing terms that account for the effect of the mean flow. Thus, the transformed transport equations are

$$\frac{\partial \rho}{\partial t} + \frac{\partial \rho u_i''}{\partial x_i} = f^{(\rho)}, \tag{22}$$

$$\frac{\partial \rho u_i''}{\partial t} + \frac{\partial \rho u_i'' u_j''}{\partial x_j} = -\frac{\partial p}{\partial x_i} + \frac{\partial t_{ij}}{\partial x_j} + f_i^{(u)}, \tag{23}$$

$$\frac{\partial \rho E}{\partial t} + \frac{\partial}{\partial x_i}\left[\rho\left(E + \frac{p}{\rho}\right)u_i''\right] = \frac{\partial u_i'' t_{ij}}{\partial x_j} - \frac{\partial q_i}{\partial x_i} + f^{(E)}, \tag{24}$$

$$\frac{\partial \rho Y_\alpha}{\partial t} + \frac{\partial \rho Y_\alpha u_i''}{\partial x_i} = -\frac{\partial J_{\alpha,i}}{\partial x_i} + f_\alpha^{(Y)}. \tag{25}$$

The forcing terms above are defined as follows

$$f^{(\rho)} = -2\rho \dot{L}, \tag{26}$$

$$f_i^{(u)} = -3\rho u_i'' \dot{L}, \tag{27}$$

$$f^{(E)} = -\left[2\rho E + \rho u_i'' u_i'' + 3p\right] \dot{L}, \tag{28}$$

$$f_\alpha^{(Y)} = -2\rho Y_\alpha \dot{L}. \tag{29}$$

L is the characteristic length of the domain, which decreases as time advances for flow compressions and increases for flow expansions. $\dot{L}$ is the constant time-rate-of-change of L.

C. Numerical details

The same numerical approach as that of Ref. [6] is used for the current study, and further details can be encountered in this reference. Direct numerical simulations are performed using the Miranda solver, which discretizes the multispecies Navier-Stokes equations using a tenth-order Padé scheme and a fourth-order Runge-Kutta integrator. Filtering of the flow variables is performed using an eight-order operator for the purposes of stability. An artificial bulk viscosity β^*, thermal conductivity κ^*, and species diffusivity D^*_α are added to the corresponding physical transport coefficients, in a similar manner to [9, 12]. The expressions for these artificial fluid properties are

$$\beta^* = \overline{c_\beta \rho D(d)}, \tag{30}$$

$$\kappa^* = \overline{c_\kappa \rho \frac{C_v}{T \Delta t} D(T)}, \tag{31}$$

$$D^*_\alpha = \overline{\rho \frac{1}{\Delta t} \max\left[c_d D(Y_\alpha), \right.} \\ \overline{\left. c_y (|Y_\alpha| - 1.0 + |1.0 - Y_\alpha|)\Delta^2\right]}. \tag{32}$$

In the above d is the dilatation, Δt is the time step, $\Delta = (\Delta x \Delta y \Delta z)^{1/3}$ is the local grid spacing, and the overline denotes a truncated-Gaussian filter. The operator $D(\cdot)$ is given by

$$D(\cdot) = \max\left(\left|\frac{\partial^8 \cdot}{\partial x^8}\right| \Delta x^{10}, \left|\frac{\partial^8 \cdot}{\partial y^8}\right| \Delta y^{10}, \left|\frac{\partial^8 \cdot}{\partial z^8}\right| \Delta z^{10} \right), \tag{33}$$

which strongly biases the artificial properties towards high wave numbers. The values of the coefficients in Eqs. (30)–(32) are $c_\beta = 0.07$, $c_\kappa = 0.001$, $c_d = 0.0002$, and $c_y = 100$, which have been calibrated using simulations relevant to ICF—see, for example, Refs. [13–15].

A cubic grid with 256^3 uniformly spaced grid points and periodic boundary conditions at all of its faces is used for the simulations. So as to be of relevance to ICF, the species chosen for the fluid mixture are hydrogen (H), deuterium (D), tritium (T), carbon (C), and oxygen (O). These species, for example, would be present in a capsule with DT fuel at its core and CRF low-density foams as the ablator [16]. The molar masses used for each of these species are $M_H = 1.00798$, $M_D = 2.014102$, $M_T = 3.016050$, $M_C = 12.0111$ and $M_O = 15.994915$. All species have the same constant Schmidt number, namely $\mathrm{Sc} = 1.0$. As shown in Ref. [17], the viscosity has a 5/2 power-law temperature scaling if other parameters such as the ionization state and the collision integrals are assumed constant. Under these assumptions, ρD also exhibits a 5/2 power-law dependence on temperature, which motivated the use of a constant Schmidt number. Simulations that account for differential diffusion, where a different Schmidt number is used for each species, did not show qualitatively different behavior even up to Schmidt numbers that differed by two orders of magnitude. Additional parameters of the simulation are the Prandtl number $\mathrm{Pr} = 1.0$, the ratio of specific heats $\gamma = 5/3$, and the universal gas constant $R_u = 8.314474 \times 10^7$ (cgs units).

D. Initial conditions

The initial condition for the velocity field was extracted from linearly-forced simulations, which have previously been shown to produce realistic fluctuating velocities [18]. Details on the implementation of this forcing mechanism, as well as the strength of the linear forcing functions that lead to DNS resolution, are included in Refs. [6, 19]. As stated in Ref. [6], compression of the initial flow field dissipates the smallest scales first, and thus an initial condition with DNS-like resolution guarantees that all of the turbulent scales are well resolved throughout the subsequent compression. The velocity field extracted from the linearly forced simulations is characterized by a turbulent Mach number $M_t \approx 0.4$ and a Taylor-scale Reynolds number $Re_\lambda \approx 50$. The TKE for this velocity field has a value of $k_0 = 2.2 \times 10^{14}$ cm/s.

Forcing functions for the mass fractions are also used in the simulations that generate the initial conditions. Rather than relying on traditional approaches based on mean scalar gradients [20, 21] or low-wavenumber forcing [22, 23], a linear scalar forcing function is used. This forcing function leads to a flow field with an averaged mass-fraction $\widetilde{Y}_\alpha$ that is constant in time and uniform in space, and a fluctuating field Y''_α that is statistically homogeneous. The linear forcing function is of the form $f^{(Y)}_\alpha = \rho c_\alpha Y''_\alpha$, and it is added to the right-hand side of the transport equation for the mass fraction of species α. The coefficient c_α is given by

$$c_\alpha = \frac{1}{2} \frac{\epsilon_{\alpha\alpha}}{\upsilon_{\alpha\alpha}}, \tag{34}$$

where $\upsilon_{\alpha\beta} = \widetilde{Y''_\alpha Y''_\beta}$ is the mass-fraction variance and $\epsilon_{\alpha\beta}$, given in Eq.(A7), is the dissipation of the mass-fraction variance. It is noted that this forcing procedure results in an initial field in which mass-fraction fluctuations of separate species are nomi-

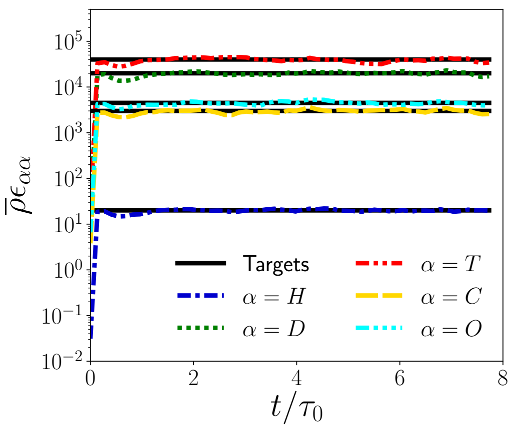

FIG. 1: Dissipation of the mass-fraction variance for the five different species simulated, compared against the target values used by the linear forcing mechanism. t is time and τ_0 is the eddy-turn-over time.

nally uncorrelated, as is the case for non-premixed materials.

The scalar forcing function used is equivalent to the second term in the forcing function introduced by Ref. [24]. The first term in the forcing function of Ref. [24], which specifies a target mass-fraction variance that the simulations ought to reach, is neglected in the current forcing scheme for the sake of simplicity. Additionally, rather than computing $\epsilon_{\alpha\alpha}$ and $\upsilon_{\alpha\alpha}$ after each time step to obtain c_α, as is done in Ref. [24], only $\upsilon_{\alpha\alpha}$ is computed in between time steps and a constant target value is used for $\epsilon_{\alpha\alpha}$. Thus, the forcing function leads to a fluctuating mass-fraction field with a variance dissipation that ought to match the predetermined target value. The agreement between the computed and target variance dissipations for the current linearly forced simulations is shown in Fig. 1.

An iteration for the target values of the mass-fraction-variance dissipation was performed until $\sqrt{\upsilon_{\alpha\alpha}}/\widetilde{Y}_\alpha \approx 40\%$ for each species. The values for the constant Favre-averaged mass fractions were computed using the molar fractions $X_H = 0.03$, $X_D = 0.455$, $X_T = 0.455$, $X_C = 0.03$, $X_O = 0.03$, which aims to roughly mimic ICF fuel contaminated by ablator components. The deuterium mass-fraction variance and the tritium-oxygen mass-fraction covariance that followed from this initialization scheme are $\upsilon_{DD,0} = 1.6 \times 10^{-2}$ and $\upsilon_{TO,0} = -3.6 \times 10^{-2}$, respectively. Since the Schmidt number used for all of the species is unity, the Batchelor scale $\phi = \eta/\mathrm{Sc}^{1/2}$ [25], which describes the smallest length scales of fluctuations in scalar concentration, is equal to the Kolmogorov scale η. Thus, the grid resolution chosen to capture all the relevant velocity scales is also appropriate for the mass-fraction field.

E. Results

The time evolution of TKE, mass-fraction variance of deuterium, and mass-fraction covariance of tritium and oxygen is shown in Fig. 2, for various compression speeds. These compression speeds are denoted by the initial value of the shear parameter $S^* = Sk/\epsilon$, where $S = \dot{L}/L$. As in Ref. [1], the evolution of the flow variables is plotted as a function of the length of the domain L, instead of time, and thus the plots in Figs. 2 are to be read from right to left. Only the mass-fraction variance of deuterium is depicted in this study, since the variances of the other four components in the fluid mixture behave in a qualitatively similar manner. Similarly, only one mass-fraction covariance is shown since the evolution of the ten covariances is qualitatively similar for the cases under consideration.

Figure 2 (a) is to be compared with Fig. 1 in [1] and Fig. 3 in [6], which show the evolution of TKE for a single-component incompressible flow and a single-component compressible flow, respectively. We note that the parameters for the single-component compressible flow ($M_t \approx 0.65$, $Re_\lambda \approx 70$) are relatively similar to those of the current multi-component compressible flow ($M_t \approx 0.4$, $Re_\lambda \approx 50$). The comparison between these three flows shows that accounting for multiple species with molecular weights that differ by up to an order of magnitude does not lead to qualitatively different TKE behavior. The sudden viscous dissipation still occurs for the multicomponent fluid mixture, and this dissipation still becomes more rapid as S_0^* is increased, in accordance to the single-component results. An extensive examination of TKE growth vs. decay for different S_0^*, as well as the critical value that demarcates these two regimes, has been previously given in the literature; see for example Sec. II B of Ref. [5] and Sec. IV A 1 of Ref. [6]. Oscillations in the TKE for the slowest compression speed, which were attributed to oscillations in the pressure-dilatation in Ref. [6], are still observed.

Of more relevance to the current study, however, is the demonstration that the mass-fraction variance also exhibits a sudden viscous dissipation, as shown in Fig. 2(b). The sudden viscous dissipa-

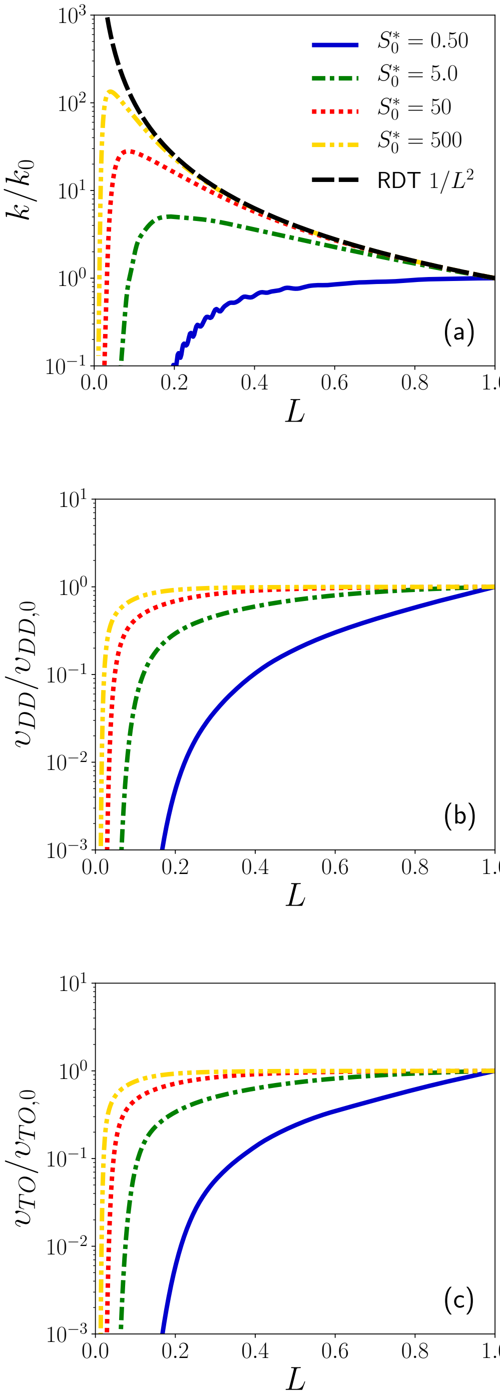

FIG. 2: Evolution of (a) turbulent kinetic energy k, (b) mass-fraction variance of deuterium υ_{DD}, and (c) mass-fraction covariance of tritium and oxygen υ_{TO}, for direct numerical simulations of isotropic compressions. The subscript $_0$ indicates initial value. The $1/L^2$ scaling in (a) follows from Rapid Distortion Theory (RDT) [26].

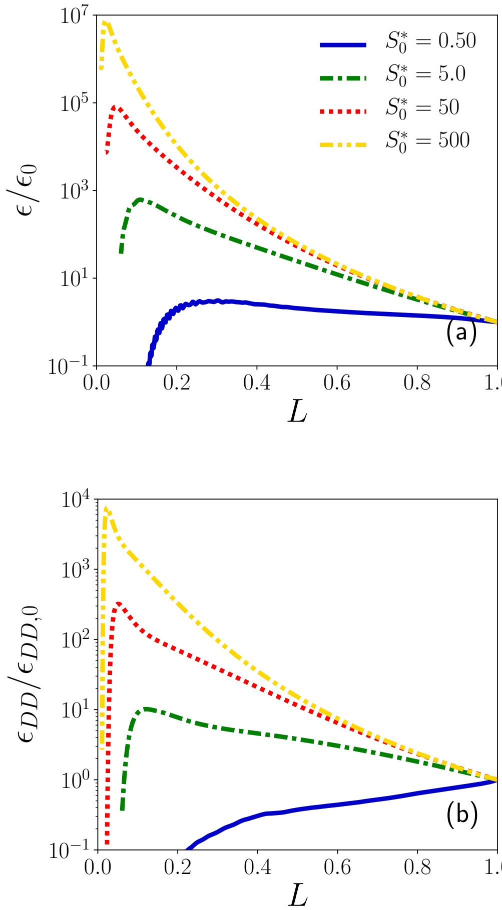

FIG. 3: Evolution of (a) TKE dissipation and (b) mass-fraction-variance dissipation, for direct numerical simulations of isotropic compressions. The subscript $_0$ indicates initial value.

tion of variance and TKE occurs at similar values of L. Additionally, in accord with the TKE, the sudden viscous dissipation of the mass-fraction variance becomes more pronounced as the compression speed is increased. Figure 2(c) shows that the mass-fraction covariance of tritium and oxygen behaves in a similar manner to the mass-fraction variance, and hence also exhibits the sudden viscous dissipation. It is noted, however, that whereas the mass-fraction variance is positive throughout the compression, the mass-fraction covariance is negative. This is not revealed by Figs. 2 (b) and 2 (c) since quantities have been normalized by their initial value.

Equation (A4) derived in the appendix shows that the evolution of the mass-fraction variance is affected by its dissipation only. Using Eq. (11) in Eq. (A7), the dissipation of mass-fraction variance for deuterium can be expressed as

$$\overline{\rho}\epsilon_{DD} = \frac{2}{\mathrm{Sc}}\overline{\mu\frac{\partial Y_D'}{\partial x_i}\frac{\partial Y_D'}{\partial x_i}}. \tag{35}$$

On the other hand, the dissipation of TKE for a homogeneous incompressible flow field [27] simplifies to

$$\overline{\rho}\epsilon = \overline{\mu\frac{\partial u_k'}{\partial x_i}\frac{\partial u_k'}{\partial x_i}}. \tag{36}$$

Due to the similarity of Eqs. (35) and (36), it is thus not surprising that the sudden viscous dissipation mechanism first demonstrated in Ref. [1] for homogeneous incompressible turbulence also applies to the mass-fraction variance. Indeed, as shown in Fig. 3, the dissipation of the mass-fraction variance behaves in a similar manner to the TKE dissipation, which for the current compressible flow is given by

$$\overline{\rho}\epsilon = \overline{\mu w_i' w_i'} + \frac{4}{3}\overline{\mu d' d'}. \tag{37}$$

In the above, $w_i' = \epsilon_{ijk}\partial u_k'/\partial x_j$ is the fluctuating vorticity vector, and $d' = \partial u_i'/\partial x_i$ is the fluctuating dilatation. For the covariance of tritium and oxygen, the dissipation is given by

$$\overline{\rho}\epsilon_{TO} = \frac{2}{\mathrm{Sc}}\overline{\mu\frac{\partial Y_T'}{\partial x_i}\frac{\partial Y_O'}{\partial x_i}}, \tag{38}$$

which also entails a product of gradients similar to those in Eq. (37).

An alternate approach for visualization of the sudden viscous dissipation of TKE and mass-fraction variance is to plot the evolution of the profiles as a function of the shear parameter, which is done in Fig. 4. As shown in Ref. [6], Figs. 4 (a) and 4 (b) divide the compression history into two regions, one dominated by TKE production to the right of the dashed vertical line, and the other dominated by TKE dissipation to the left. This vertical line denotes the point in time at which TKE production equals TKE dissipation. As shown in Fig. 4 (b), no production of mass-fraction variance is present to the right of the vertical dashed line, whereas the dissipative decay does occur on the left-hand side. These two figures also include fiducials as diagonal dashed black lines, with a slope of 2.8 in Fig. 4 (a) and 3.3 in Fig. 4 (b). These fiducials are used to gauge the rate of decay as a function of S^* of both k and υ_{DD}.

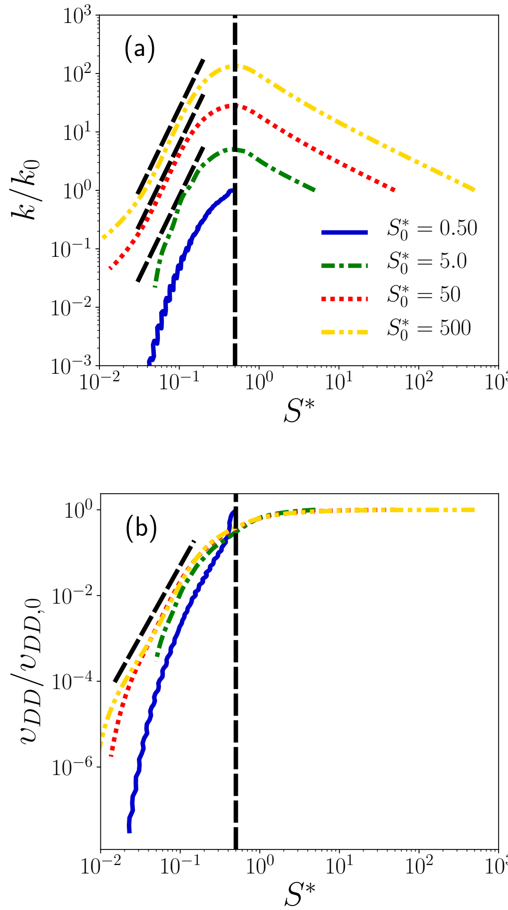

FIG. 4: Evolution of (a) turbulent kinetic energy k and (b) mass-fraction variance of deuterium υ_{DD}, for direct numerical simulations of isotropic compressions. The vertical dashed line corresponds to the point in time at which production and dissipation of turbulent kinetic energy are equal. The diagonal dashed lines serve as fiducials, with a slope of 2.8 in (a) and 3.3 in (b). The subscript $_0$ indicates initial value.

Additional direct numerical simulations of isotropic compressions were carried out using different values for the power-law coefficient, as was done in Ref. [4]. Results from these simulations are given in Fig. 5, which shows again that the TKE, mass-fraction variance, and mass-fraction covariance exhibit the sudden viscous dissipation. Additionally, direct numerical simulations of an isotropic expansion were carried out for multiple values of the initial shear parameter, and results

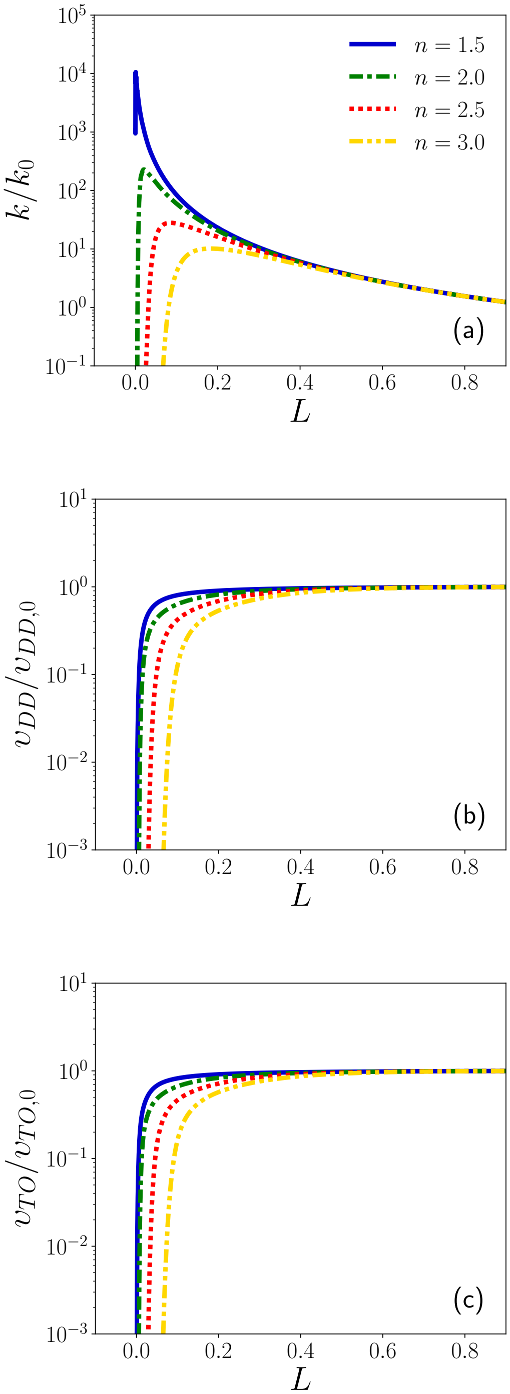

FIG. 5: Evolution of (a) turbulent kinetic energy k, (b) mass-fraction variance of deuterium v_{DD}, and (c) mass-fraction covariance of tritium and oxygen v_{TO}, for direct numerical simulations of isotropic compressions. n is the power-law exponent, and the subscript $_0$ indicates initial value.

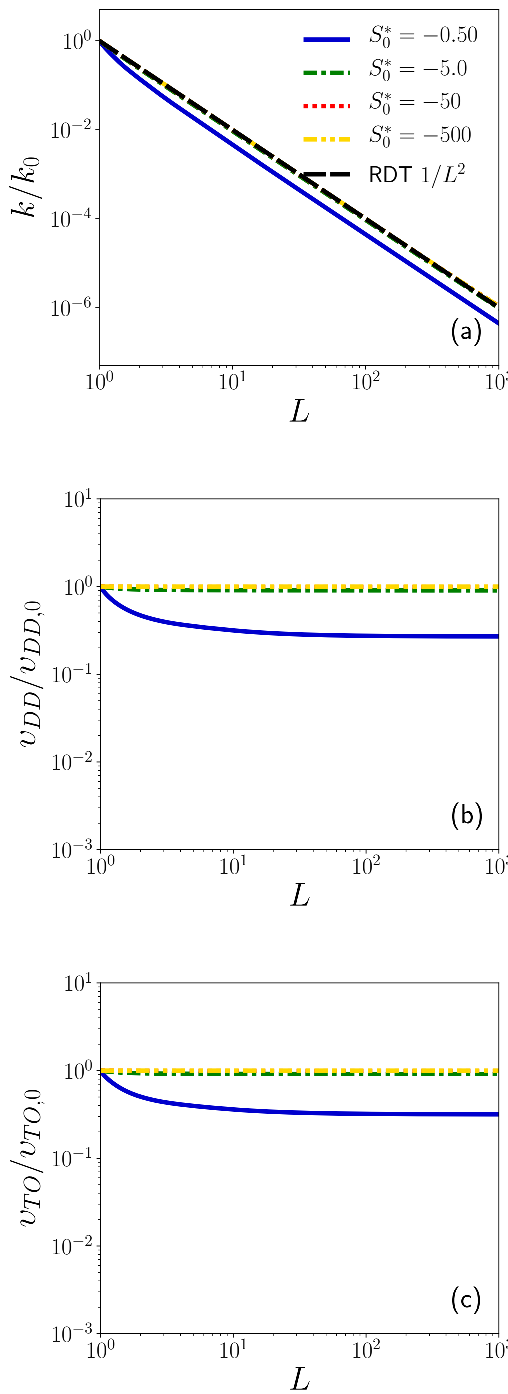

FIG. 6: Evolution of (a) turbulent kinetic energy k, (b) mass-fraction variance of deuterium v_{DD}, and (c) mass-fraction covariance of tritium and oxygen v_{TO}, for direct numerical simulations of isotropic expansions. The subscript $_0$ indicates initial value. The $1/L^2$ scaling in (a) follows from Rapid Distortion Theory (RDT) [26].

are given in Fig. 6. For this new case, the sudden viscous dissipation mechanism is inactive, since the expansion leads to a continuous decrease of temperature and thus the viscosity does not reach sufficiently large values to suddenly precipitate the dissipative decay. As is the case for simulations of compressed turbulence with various values of S_0^*, the variance and covariance for these two new cases are of opposite sign, and their normalized magnitudes evolve in an equal manner. All three sets of simulations (compression with varying S_0^*, compression with varying n, and expansion with varying S_0^*) are used in the following section to validate the original and modified RANS formulations.

III. REYNOLDS-AVERAGED NAVIER-STOKES MODELING

A. Governing equations for isotropic deformations

The Reynolds-averaged Navier-Stokes equations, which are summarized in Appendix B for a generic flow, simplify significantly for homogeneous turbulence with isotropic deformations. For the mean flow, the density is given by $\overline{\rho} = \overline{\rho}_0 L^{-3}$, where $\overline{\rho}_0$ is the initial averaged density, and the averaged velocity is determined from the deformation tensor $G_{ij} = \partial\widetilde{u}_i/\partial x_j$. For isotropic compressions and expansions this tensor takes the form $G_{ij} = (\dot{L}/L)\delta_{ij}$. The evolution of the internal energy is given by

$$\overline{\rho}\frac{\partial\widetilde{e}}{\partial t} = -\overline{p}G_{ii} - \overline{p'\frac{\partial u_i'}{\partial x_i}} + C_D\overline{\rho}\frac{(2k)^{3/2}}{l_d}, \qquad (39)$$

which follows from Eq. (B3). Since a uniform distribution for the averaged mass fraction $\widetilde{Y}_\alpha$ is used as an initial condition, $\widetilde{Y}_\alpha$ remains constant and uniform across time and space, as can be deduced from Eq. (B4). Additional relations for the mean flow given in Sec. B 1 still hold.

Due to the isotropy of G_{ij}, the Reynolds stresses are modeled simply as $\tau_{ij} = (2/3)k\delta_{ij}$. Moreover, since both $\widetilde{T}$ and $\widetilde{Y}_\alpha$ are uniform, the internal-energy turbulent flux given by Eq. (B23) and the species turbulent flux given by Eq. (B24) are both zero.

The transport equations for the turbulent variables also simplify significantly for homogeneous turbulence with isotropic mean-flow deformations. Foremost, only the dissipative length scale l_d is needed since the transport length scale l_t is used exclusively for the modeling of the deviatoric component of the Reynolds stresses, which is zero for this case. Additionally, due to the spatial uniformity of $\overline{p}$, and the fact that $\overline{t}_{ij}$ is equal to zero, the mass-weighted velocity fluctuation does not appear in the internal energy equation, and thus the equation for a_i is not required. As a result, the transport equations needed to simulate the isotropic compression and expansion are

$$\frac{dk}{dt} = -\frac{2}{3}kG_{kk} - C_D\frac{(2k)^{3/2}}{l_d}, \qquad (40)$$

$$\frac{dl_d}{dt} = C_{l1}\sqrt{2k} - \frac{2}{3}C_{l2d}l_dG_{kk}, \qquad (41)$$

$$\frac{d\upsilon_{\alpha\beta}}{dt} = -C_{\upsilon 2}\frac{\sqrt{2k}}{l_d}\upsilon_{\alpha\beta}. \qquad (42)$$

Out of the entire set of coefficients given in Eq. (B33), only the following are now required

$$\begin{aligned} C_D = 0.354 \quad & C_{l1} = 0.283 \\ C_{l2d} = 0.272 \quad & C_{\upsilon 2} = 0.849. \end{aligned} \qquad (43)$$

B. Modifications to the k-l_d model

The changes in the original k-l_d model are based on previous modifications to the k-ϵ model that led to improved prediction of compressed turbulence. The first modification introduces an alternate form of the production term in the transport equation for the dissipative length scale. We start by noting that the traditional model for the TKE dissipation ϵ [28–30] contains the following production term

$$\frac{d\epsilon}{dt} = -C_{\epsilon 1}\frac{\epsilon}{k}\tau_{ij}\frac{\partial\widetilde{u}_i}{\partial x_j} + ... \qquad (44)$$

The coefficient $C_{\epsilon 1}$ is typically set to 1.44. Given the relationship $l_d = C_D(2k)^{3/2}/\epsilon$, one can use the transport equations for k and ϵ to derive an equation for the length scale [31]. The corresponding production term in the l_d equation would be as follows

$$\frac{dl_d}{dt} = -\left(\frac{3}{2} - C_{\epsilon 1}\right)\tau_{ij}\frac{l_d}{k}\frac{\partial\widetilde{u}_i}{\partial x_j} + ... \qquad (45)$$

This is the form of the production term that is used in Refs. [9, 10, 31, 32], albeit with different coefficients. The exact transport equation for ϵ [33] contains both an explicit dilatational term and a deviatoric production term—this deviatoric production depends solely on the deviatoric Reynolds stress $\tau_{ij}^{(d)}$.

Thus, Ref. [33] suggested the use of the following instead of the original production in Eq. (44)

$$\frac{d\epsilon}{dt} = -C_{\epsilon 1}\frac{\epsilon}{k}\tau_{ij}^{(d)}\frac{\partial \widetilde{u}_i}{\partial x_j} - \frac{2}{3}C_{\epsilon 3}\epsilon\frac{\partial \widetilde{u}_k}{\partial x_k} + ... \tag{46}$$

For the above, $C_{\epsilon 3} = 2.0$ so as to match the dilatational term in the exact transport equation for dissipation. This replacement of the traditional production then leads to the following in the l_d equation

$$\frac{dl_d}{dt} = -\left(\frac{3}{2} - C_{\epsilon 1}\right)\tau_{ij}^{(d)}\frac{l_d}{k}\frac{\partial \widetilde{u}_i}{\partial x_j} - \left(1 - \frac{2}{3}C_{\epsilon 3}\right)l_d\frac{\partial \widetilde{u}_k}{\partial x_k} + ... \tag{47}$$

The decomposition of the production into isotropic and deviatoric components as shown above allows for greater flexibility in the k-l family of models. As shown in Ref. [10], a production term of the form $\tau_{ij}(l_d/k)\partial\widetilde{u}_i/\partial x_j$ in the l_d equation is critical for the appropriate representation of Kelvin-Helmholtz mixing layers. Instead of using the coefficient $-(3/2 - C_{\epsilon 1})$ as shown in Eq. (45), the coefficient $C_{l2d} = 0.272$ was used in Ref. [10] to obtain self-similar solutions. However, a single production term with a coefficient C_{l2d} for the l_d equation as in Eq. (45) does not allow for the accurate prediction of mean-flow compression and expansion. With the decomposition of production into deviatoric and isotropic components, the coefficient C_{l2d} can still be used for the first term on the right-hand-side of Eq. (47), and the coefficient $C_{\epsilon 3}$ can be used in the second-term on the right-hand side of Eq. (47). That is

$$\frac{dl_d}{dt} = -C_{l2d}\tau_{ij}^{(d)}\frac{l_d}{k}\frac{\partial \widetilde{u}_i}{\partial x_j} - \left(1 - \frac{2}{3}C_{\epsilon 3}\right)l_d\frac{\partial \widetilde{u}_k}{\partial x_k} + ... \tag{48}$$

Thus, the first term on the right-hand-side above allows for the self-similar solutions of the Kelvin-Helmholtz mixing layer described in [10], and the second term on the right-hand-side above allows for accurate predictions of mean-flow compressions and expansions.

The second modification to the k-l_d model is the addition of a variable-viscosity term in the l_d equation. To improve predictions of isotropic rapid compressions, Ref. [34] suggested the addition of the term $(\epsilon/\nu)d\nu/dt$ to the dissipation evolution equation, where $\nu = \mu/\rho$. This approach led to time-evolutions of the dissipation in agreement with a low-Mach-number DNS, and is simpler than the three-equation model formulated by Ref. [3]. Given an evolution equation for dissipation that includes the variable-viscosity term, the corresponding evolution equation for l_d obtained from the relationship $l_d = C_D(2k)^{3/2}/\epsilon$ includes the additional term $-(l_d/\nu)d\nu/dt$.

Using the two modifications described above, the original l_d Eq. (41) is replaced by

$$\frac{dl_d}{dt} = C_{l1}\sqrt{2k} - \left(1 - \frac{2}{3}C_{\epsilon 3}\right)l_d G_{kk} - \frac{l_d}{\nu}\frac{d\nu}{dt}. \tag{49}$$

Note the difference between the coefficients in front of the second term on the right-hand side of Eqs. (41) and (49), namely, $(2/3)C_{l2d}$ vs. $[1-(2/3)C_{\epsilon 3}]$. These two terms differ not only in value but also in sign, i.e. 0.181 vs. $-1/3$. Again, it is noted that for a more general case in which shear is also present, both C_{l2d} and $C_{\epsilon 3}$ are used to model production, according to Eq. (48). Additionally, we note that the two modifications implemented in the l_d evolution equation follow from modifications to the evolution equation for the solenoidal dissipation $\rho\epsilon = \overline{\mu w_i' w_i'}$, where w_i' is the fluctuating vorticity vector. For flows with large Mach numbers, the dilatational dissipation [33, 35] cannot be neglected. However, as stated in [33], a simple model for the dilatational dissipation is $M_t^2\epsilon$. Since for the current simulations $M_t^2 \approx 0.15$, it is expected that the dilatational dissipation would play a small role on the overall statistics.

C. Results

Equations (39), (40), (41) and (42) constitute the original k-l formulation. For the modified k-l model, Eq. (41) is replaced by Eq. (49). These ordinary differential equations are integrated forward in time using a second-order Runge Kutta scheme, with initial conditions that are extracted from the DNS.

Figure 7 shows predictions of TKE, mass-fraction variance, and mass-fraction covariance obtained with the original (left column) and modified (right column) k-l models, for isotropic compressions with various initial values of S^*. This figure is thus meant to be compared against the DNS results of Fig. 2. Figs. 7(a), 7(c) and 7(e) demonstrate the poor prediction of the original k-l model given in Sec. III A. This formulation predicts increasing values of TKE at all domain lengths and for all compression speeds, and is thus unable to reproduce the sudden viscous dissipation exhibited by the DNS results. For the mass-fraction variance and covariance, the original model predicts rates of decay that are not as strong or rapid as those obtained with DNS. On the other

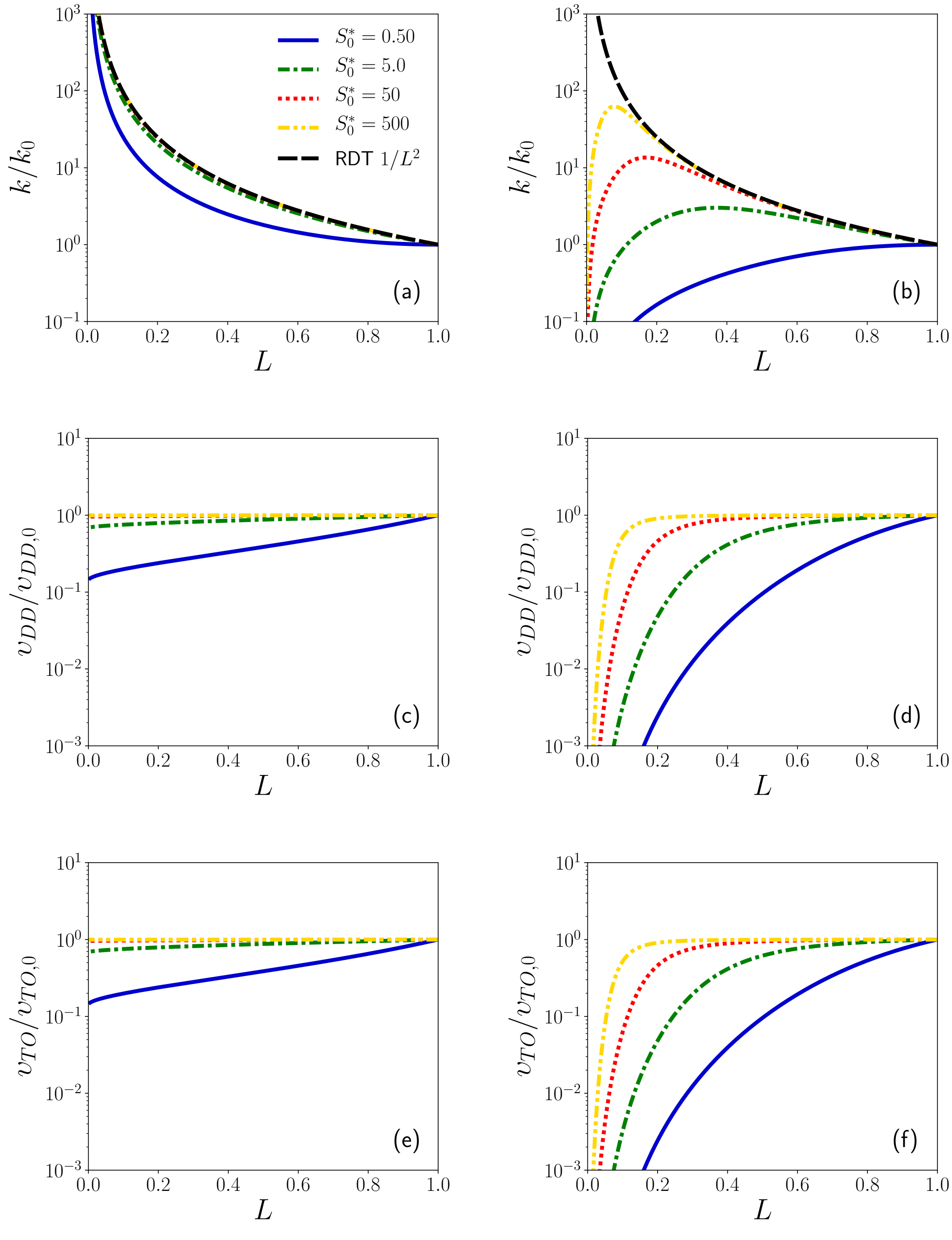

FIG. 7: Evolution of turbulent kinetic energy k on the top row, mass-fraction variance of deuterium υ_{DD} on the middle row, and mass-fraction covariance of tritium and oxygen υ_{TO} on the bottom row, for RANS simulations of isotropic compressions. Left column, original k-l_d; right column, modified k-l_d. The subscript $_0$ indicates initial value. The $1/L^2$ scaling in (a) and (b) follows from Rapid Distortion Theory (RDT) [26].

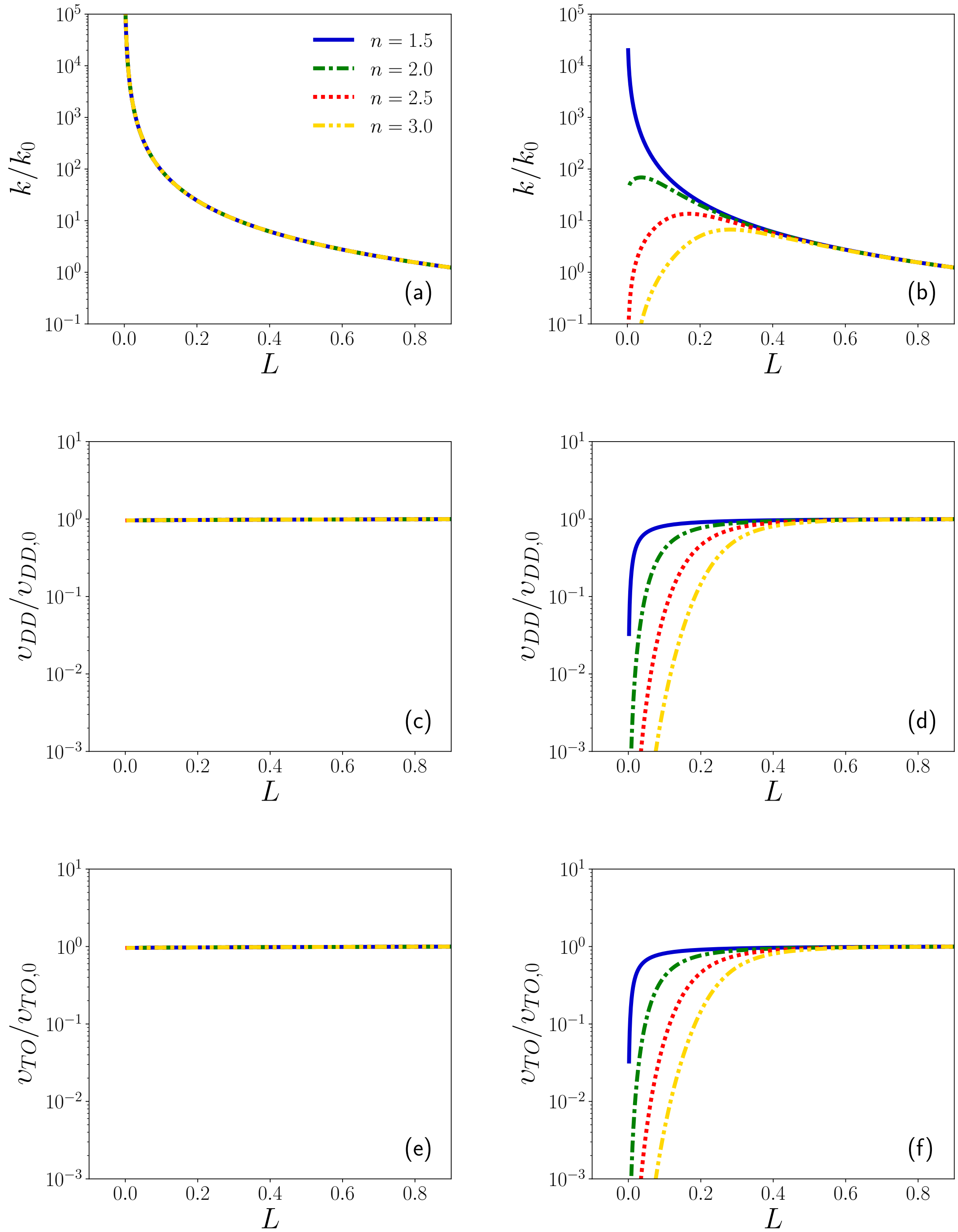

FIG. 8: Evolution of turbulent kinetic energy k on the top row, mass-fraction variance of deuterium v_{DD} on the middle row, and mass-fraction covariance of tritium and oxygen v_{TO} on the bottom row, for RANS simulations of isotropic compressions. Left column, original k-l_d; right column, modified k-l_d. n is the power-law exponent, and the subscript $_0$ indicates initial value.

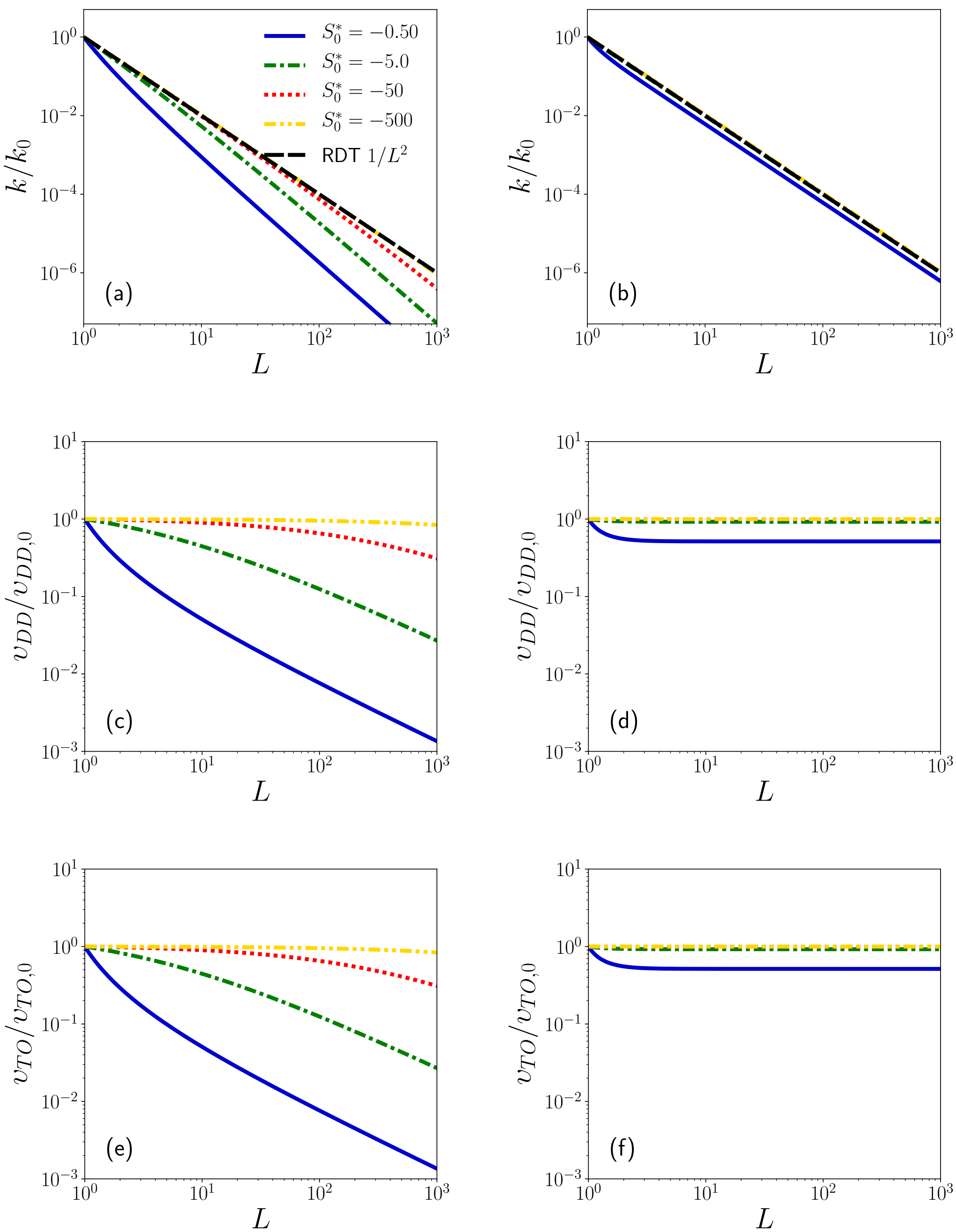

FIG. 9: Evolution of turbulent kinetic energy k on the top row, mass-fraction variance of deuterium υ_{DD} on the middle row, and mass-fraction covariance of tritium and oxygen υ_{TO} on the bottom row, for RANS simulations of isotropic expansions. Left column, original k-l_d; right column, modified k-l_d. The subscript $_0$ indicates initial value. The $1/L^2$ scaling in (a) and (b) follows from Rapid Distortion Theory (RDT) [26].

hand, the new version of the k-l model from Sec. III B gives significantly improved predictions compared to the original formulation. This new model is able to capture the sudden viscous dissipation of TKE, mass-fraction variance, and mass-fraction covariance, for all compression speeds. A perfect agreement with DNS is not achieved, since the sudden dissipation is slightly sharper for the DNS than the model. Nonetheless, the evolution of each k, υ_{DD}, and υ_{TC} profile, as well as the overall trend exhibited as the compression speed is varied, are both adequately reproduced. We do emphasize that Eq. (42) is based on the k-l model of Ref. [9], which is intended for binary mixing and thus has neither been designed nor formulated to capture covariances. As can be deduced from Eq. (42), the same temporal evolution is obtained for normalized variances and covariances $\upsilon_{\alpha\beta}/\upsilon_{\alpha\beta,0}$. For this specific case, the model is in agreement with the DNS since the evolutions of the normalized variance and covariance extracted from the DNS are, although not exactly equal to each other, almost identical.

Figure 8 shows TKE, mass-fraction variance, and mass-fraction covariance predicted by the original (left column) and modified (right column) k-l models, for isotropic compressions with various values of the viscosity power-law exponent n. This figure is thus meant to be compared against the DNS results of Fig. 5. As for the previous case, the evolution of k, υ_{DD}, and υ_{TC} predicted by the original k-l model does not exhibit the sudden viscous dissipation mechanism; instead all TKE profiles grow indefinitely at an equal rate and the variance and covariance remain constant. On the other hand, the the modified k-l model is able to capture the sudden decay in k, υ_{DD}, υ_{TC}. As was the case for the simulations in which the compression rate was varied, the k-l models predict the same evolution for normalized variance and covariance. We note that the RANS simulations using the original and modified k-l models were both carried out up to the smallest values of L that could be reached before encountering numerical instabilities. This value of L for the $n = 1.5$ case is $L \approx 1.8 \times 10^{-3}$, which is about an order of magnitude larger than that reached with the DNS, namely, $L \approx 9.4 \times 10^{-5}$. This, in part, explains why by this last instance in time the TKE predicted by the new k-l formulation for the $n = 1.5$ case has not yet started to decay, as is the case for the DNS shown in Fig. 5. Additionally, as previously stated, the sudden viscous dissipation predicted by DNS is still slightly sharper, or more abrupt, than that obtained with the new k-l model. Nonetheless, the trend exhibited by k, υ_{DD}, and υ_{TC} as the power-law-exponent is varied is appropriately captured by the new model, and is entirely missed by the original k-l formulation.

Figure 9 shows predictions of TKE, mass-fraction variance, and mass-fraction covariance, obtained with the original (left column) and modified (right column) k-l models, for isotropic expansions with various initial values of S^*. This figure is thus meant to be compared against the DNS results of Fig. 6. As for previous cases, the new model provides improved predictions for k, υ_{DD}, and υ_{TC} compared to the original k-l formulation. The DNS results of Fig. 6 show that, for each flow variable, the three fastest expansion speeds lead to the same profile evolution, and it is only the profile for the slowest expansion that differs from the other three. This behavior is reproduced with the new k-l model, as shown in Figs. 9 (b), 9 (d), and 9 (f). On the other hand, Figs. 9 (a), 9 (c), and 9 (e) show that the original k-l formulation gives dissimilar decay rates for each of the expansion speeds, and these decay rates are too fast compared to the DNS results. A shortcoming of the new k-l model for this case is that it does not predict as large of a decay of υ_{DD} and υ_{TC} compared to the DNS, for the slowest expansion. Similar to the results shown in Figs. 7 and 8, the models predict the same evolution for the variance and covariance.

IV. CONCLUSIONS

An extension of previous work is carried out by simulating the sudden viscous dissipation mechanism of a multicomponent, rather than a single component, fluid. Direct numerical simulations of a five component mixture have shown that the sudden viscous dissipation of TKE is essentially unchanged for the multicomponent case when compared against the single-species results reported in Refs. [1, 6]. The DNS data also shows that the mass-fraction variance and covariance do exhibit a sudden viscous dissipative decay in a similar fashion to that of the TKE.

The latest iteration in the family of k-l RANS models, which reproduces self-similar solutions of buoyancy-, shock-, and shear-driven instabilities of relevance to ICF, has been used as the baseline to be modified so as to improve predictions of the sudden viscous dissipation. Thus, it is hoped that these modified closures can eventually be used to perform simulations of ICF capsules that simultaneously account for fluid instabilities and the sudden viscous dissipation. The modifications to the model developed in this paper consist of an alternate length-scale production and the addition of a variable-viscosity term. The modified length-scale production results from splitting the original production into two terms, one that depends on the anisotropy of the Reynolds stresses rather than the full tensor, and another that follows from the dilatational term present in the exact equation of the TKE dissipation. The variable viscosity term, on the other hand, is required so that the modeled transport equations can directly capture unexpected viscous effects that result from non-standard viscosity models. Whereas the original baseline k-l model performs quite poorly at predicting the sudden viscous dissipation of TKE and mass-fraction variance and covariance, significantly improved agreement with DNS data is obtained when both of the modifications previously described are implemented. The RANS models also show that the simple closure used for the dissipation of variance and covariance leads to the same dynamical behavior for these two quantities. Although for this case this is in agreement with DNS, for other flow scenarios with alternate initial conditions dissimilar models for the variance and covariance may be needed.

As stated in Refs. [1] and [6], additional physical phenomena such as alternate compression histories, complex transport coefficients, nuclear reactions, and the dissipation of non-turbulent motions still need to be explored to reliably gauge the utility of the sudden viscous dissipation mechanism for ICF. For example, tabular equations of state for high-energy-density regimes are needed to replace the currently used ideal equations of state. A subset of simulations previously carried out for a deuterium tritium mixture with the LEOS equation of state (https://wci.llnl.gov/simulation/support-libraries) did not show notable differences for the sudden viscous dissipation. Still, further simulations with complex equations of state need to be carried out. Similarly, it is yet unknown what effect a real-plasma model for the diffusive flux that accounts for the Soret effect, Barodiffusion, isotopic separation, etc. would have on the sudden viscous dissipation mechanism. Nonetheless, the current work serves as a further step in increasing the physical fidelity of simulations, so as to continually build on the original work of Ref. [1] for incompressible single-species turbulence. The inclusion of multiple species now paves the way forward for future simulations with multi-component transport coefficients and thermonuclear fusion reactions.

V. ACKNOWLEDGMENTS

This work was performed under the auspices of the U.S. Department of Energy by Lawrence Livermore National Laboratory under Contract DE-AC52-07NA27344.

Appendix A: Exact transport equation for mass-fraction variance

The exact transport equation for the mass-fraction variance $\upsilon_{\alpha\beta} = \widetilde{Y''_\alpha Y''_\beta}$ is

$$\frac{\partial \overline{\rho}\upsilon_{\alpha\beta}}{\partial t} + \frac{\partial \overline{\rho}\upsilon_{\alpha\beta}\widetilde{u}_i}{\partial x_j} = -\overline{Y''_\alpha}\frac{\partial \overline{J}_{\beta,i}}{\partial x_i} - \overline{Y''_\beta}\frac{\partial \overline{J}_{\alpha,i}}{\partial x_i} - \overline{\rho}\widetilde{Y''_\beta u''_i}\frac{\partial \widetilde{Y}_\alpha}{\partial x_i} - \overline{\rho}\widetilde{Y''_\alpha u''_i}\frac{\partial \widetilde{Y}_\beta}{\partial x_i} + \overline{J'_{\beta,i}\frac{\partial Y'_\alpha}{\partial x_i}} + \overline{J'_{\alpha,i}\frac{\partial Y'_\beta}{\partial x_i}} - \frac{\partial}{\partial x_i}\left(\overline{\rho}\,\widetilde{Y''_\alpha Y''_\beta u''_i} + \overline{Y'_\alpha J'_{\beta,i}} + \overline{Y'_\beta J'_{\alpha,i}}\right) \quad \text{(A1)}$$

The dissipation $\epsilon_{\alpha\beta}$ of the mass-fraction variance is defined as

$$\overline{\rho}\epsilon_{\alpha\beta} = -\overline{J'_{\beta,i}\frac{\partial Y'_\alpha}{\partial x_i}} - \overline{J'_{\alpha,i}\frac{\partial Y'_\beta}{\partial x_i}}. \quad \text{(A2)}$$

For homogeneous turbulence and spatially-uniform values of $\widetilde{Y}_\alpha$, which is the case under consideration, Eq. (A1) becomes

$$\overline{\rho}\frac{d\upsilon_{\alpha\beta}}{dt} = -\overline{Y''_\alpha}\frac{\partial \overline{J}_{\beta,i}}{\partial x_i} - \overline{Y''_\beta}\frac{\partial \overline{J}_{\alpha,i}}{\partial x_i} - \overline{\rho}\epsilon_{\alpha\beta}. \quad \text{(A3)}$$

Given the model for the averaged diffusive flux in Eq. (B7), the first and second terms in Eq. (A3) are equal to zero, and thus

$$\frac{d\upsilon_{\alpha\beta}}{dt} = -\epsilon_{\alpha\beta}. \quad \text{(A4)}$$

Since $J'_{\alpha,i} = J_{\alpha,i} - \overline{J}_{\alpha,i}$, the mass-fraction variance dissipation can be written as

$$\overline{\rho}\epsilon_{\alpha\beta} = -\overline{J_{\beta,i}\frac{\partial Y'_\alpha}{\partial x_i}} - \overline{J_{\alpha,i}\frac{\partial Y'_\beta}{\partial x_i}}. \quad \text{(A5)}$$

Using the definition of the scalar diffusive flux in Eq. (7), the above becomes

$$\overline{\rho}\epsilon_{\alpha\beta} = \overline{\rho D\frac{\partial Y_\beta}{\partial x_i}\frac{\partial Y'_\alpha}{\partial x_i}} + \overline{\rho D\frac{\partial Y_\alpha}{\partial x_i}\frac{\partial Y'_\beta}{\partial x_i}}. \quad \text{(A6)}$$

Given the spatial uniformity of $\widetilde{Y}_\alpha$, the mass-fraction dissipation is finally expressed as

$$\overline{\rho}\epsilon_{\alpha\beta} = \overline{2\rho D\frac{\partial Y'_\alpha}{\partial x_i}\frac{\partial Y'_\beta}{\partial x_i}}. \quad \text{(A7)}$$

Appendix B: Reynolds-averaged Navier-Stokes equations for a generic flow

1. The mean flow

In this section we summarize the equations that result from averaging the multicomponent Navier-Stokes equations described in Sec. II A. The transport partial differential equations for the averaged density, velocity, internal energy, and species mass fraction are

$$\frac{\partial \overline{\rho}}{\partial t} + \frac{\partial \overline{\rho}\widetilde{u}_i}{\partial x_i} = 0, \tag{B1}$$

$$\frac{\partial \overline{\rho}\widetilde{u}_i}{\partial t} + \frac{\partial \overline{\rho}\widetilde{u}_i\widetilde{u}_j}{\partial x_j} = -\frac{\partial \overline{p}}{\partial x_i} + \frac{\partial \overline{t}_{ij}}{\partial x_j} - \frac{\partial \overline{\rho}\tau_{ij}}{\partial x_j}, \tag{B2}$$

$$\begin{aligned} \frac{\partial \overline{\rho}\widetilde{e}}{\partial t} + \frac{\partial \overline{\rho}\widetilde{e}\widetilde{u}_j}{\partial x_j} &= -\overline{p}\frac{\partial \widetilde{u}_i}{\partial x_i} + \overline{t}_{ij}\frac{\partial \widetilde{u}_i}{\partial x_j} \\ &\quad + \overline{u''}_i\frac{\partial \overline{p}}{\partial x_i} - \overline{u''}_i\frac{\partial \overline{t}_{ij}}{\partial x_j} - \overline{p'\frac{\partial u_i'}{\partial x_i}} + \overline{t_{ij}'\frac{\partial u_i'}{\partial x_j}} \\ &\quad - \frac{\partial}{\partial x_j}\left(\overline{\rho}\widetilde{e''u_j''} + \overline{u''}_j\overline{p} - \overline{u''}_i\overline{t}_{ij} + \overline{q}_j\right), \end{aligned} \tag{B3}$$

$$\frac{\partial \overline{\rho}\widetilde{Y}_\alpha}{\partial t} + \frac{\partial \overline{\rho}\widetilde{Y}_\alpha\widetilde{u}_i}{\partial x_i} = -\frac{\partial \overline{J}_{\alpha,i}}{\partial x_i} - \frac{\partial \overline{\rho}\widetilde{Y_\alpha''u_j''}}{\partial x_j}. \tag{B4}$$

For the above, $\tau_{ij} = \widetilde{u_i''u_j''}$ represents the Reynolds stresses. The averaged fluxes are computed as follows

$$\overline{t}_{ij} = 2\mu\widetilde{S}_{ij} + \left(\beta - \frac{2}{3}\mu\right)\frac{\partial \widetilde{u}_k}{\partial x_k}\delta_{ij}, \tag{B5}$$

$$\overline{q}_i = -\kappa\frac{\partial \widetilde{T}}{\partial x_i}, \tag{B6}$$

$$\overline{J}_{\alpha,i} = -\overline{\rho}D\frac{\partial \widetilde{Y}_\alpha}{\partial x_i}. \tag{B7}$$

Fluctuations of the transport coefficients are neglected. These coefficients are computed using

$$\mu = \mu_0\left(\frac{\widetilde{T}}{T_0}\right)^n, \tag{B8}$$

$$\kappa = \frac{\mu\widetilde{C}_p}{\mathrm{Pr}}, \tag{B9}$$

$$D = \frac{\mu}{\overline{\rho}\mathrm{Sc}}. \tag{B10}$$

Each species is treated as an ideal gas, and thus it is assumed that averaged quantities satisfy

$$\overline{p}_\alpha = \overline{\rho}_\alpha R_\alpha \widetilde{T}, \tag{B11}$$

$$R_\alpha = \frac{R_u}{M_\alpha}, \tag{B12}$$

$$\widetilde{e}_\alpha = C_{v,\alpha}\widetilde{T}, \tag{B13}$$

$$\widetilde{h}_\alpha = C_{p,\alpha}\widetilde{T}. \tag{B14}$$

From the averaged properties of the individual species one can obtain averaged quantities for the entire mixture using

$$\widetilde{e} = \sum_\alpha \widetilde{Y}_\alpha\widetilde{e}_\alpha \qquad \widetilde{C}_v = \sum_\alpha \widetilde{Y}_\alpha C_{v,\alpha}, \tag{B15}$$

$$\widetilde{h} = \sum_\alpha \widetilde{Y}_\alpha\widetilde{h}_\alpha \qquad \widetilde{C}_p = \sum_\alpha \widetilde{Y}_\alpha C_{p,\alpha}, \tag{B16}$$

$$\overline{p} = \sum_\alpha \overline{V}_\alpha\overline{p}_\alpha \qquad \overline{V}_\alpha = \frac{\overline{\rho}\widetilde{Y}_\alpha}{\overline{\rho}_\alpha}. \tag{B17}$$

Finally, additional relationships are

$$\widetilde{E} = \widetilde{e} + \bar{K} + k, \tag{B18}$$

$$\bar{K} = \frac{1}{2}\widetilde{u}_i\widetilde{u}_i, \tag{B19}$$

$$k = \frac{1}{2}\widetilde{u_i''u_i''}, \tag{B20}$$

$$\widetilde{S}_{ij} = \frac{1}{2}\left(\frac{\partial \widetilde{u}_i}{\partial x_j} + \frac{\partial \widetilde{u}_j}{\partial x_i}\right). \tag{B21}$$

2. The k-2l-a-υ model

Due to the lack of closure in the mean flow equations of Sec. B 1, a turbulence model is required. The latest iteration in the family [9, 10, 36, 37] of

k-l models is used in this study, namely the k-2l-a-υ model.

The turbulent fluxes are modeled using

$$\overline{\rho}\tau_{ij} = \frac{2}{3}\overline{\rho}k\delta_{ij} - C_{dev}2\mu_t\left(\widetilde{S}_{ij} - \frac{1}{3}\widetilde{S}_{kk}\delta_{ij}\right), \quad \text{(B22)}$$

$$\overline{\rho}\widetilde{e''u_j''} = -\frac{\kappa_t}{\widetilde{\gamma}}\frac{\partial \widetilde{T}}{\partial x_j}, \quad \text{(B23)}$$

$$\overline{\rho}\widetilde{Y_\alpha''u_j''} = -\overline{\rho}D_t\frac{\partial \widetilde{Y}_\alpha}{\partial x_j}. \quad \text{(B24)}$$

Note that for the above, $\widetilde{\gamma} = \widetilde{C}_p/\widetilde{C}_v$. The modeled turbulent fluxes above depend on eddy transport coefficients, which are given below

$$\mu_t = C_\mu\overline{\rho}\sqrt{2k}l_t, \quad \text{(B25)}$$

$$\kappa_t = \frac{\mu_t\widetilde{C}_p}{\mathrm{Pr}_t}, \quad \text{(B26)}$$

$$D_t = \frac{\mu_t}{\overline{\rho}\mathrm{Sc}_t}. \quad \text{(B27)}$$

The transport equations of the model are

$$\frac{\partial\overline{\rho}k}{\partial t} + \frac{\partial\overline{\rho}k\widetilde{u}_i}{\partial x_i} = -\overline{\rho}\tau_{ij}\frac{\partial\widetilde{u}_i}{\partial x_j} - C_D\overline{\rho}\frac{(2k)^{3/2}}{l_d} + \frac{\partial}{\partial x_i}\left[\left(\mu + \frac{\mu_t}{N_k}\right)\frac{\partial k}{\partial x_i}\right], \quad \text{(B28)}$$

$$\frac{\partial\overline{\rho}l_t}{\partial t} + \frac{\partial\overline{\rho}l_t\widetilde{u}_i}{\partial x_i} = C_{l1}\overline{\rho}\sqrt{2k} - C_{l2t}\overline{\rho}\tau_{ij}\frac{l_t}{k}\frac{\partial\widetilde{u}_i}{\partial x_j} + \frac{\partial}{\partial x_i}\left[\left(\mu + \frac{\mu_t}{N_{lt}}\right)\frac{\partial l_t}{\partial x_i}\right], \quad \text{(B29)}$$

$$\frac{\partial\overline{\rho}l_d}{\partial t} + \frac{\partial\overline{\rho}l_d\widetilde{u}_i}{\partial x_i} = C_{l1}\overline{\rho}\sqrt{2k} - C_{l2d}\overline{\rho}\tau_{ij}\frac{l_d}{k}\frac{\partial\widetilde{u}_i}{\partial x_j} + \frac{\partial}{\partial x_i}\left[\left(\mu + \frac{\mu_t}{N_{ld}}\right)\frac{\partial l_d}{\partial x_i}\right], \quad \text{(B30)}$$

$$\frac{\partial\overline{\rho}a_i}{\partial t} + \frac{\partial\overline{\rho}a_i\widetilde{u}_i}{\partial x_i} = C_B^2 b\frac{\partial\overline{p}}{\partial x_i} - C_a\overline{\rho}a_i\frac{\sqrt{2k}}{l_d} - \overline{\rho}\tau_{ij}\frac{\partial\overline{\rho}}{\partial x_j} + \frac{\partial}{\partial x_j}\left[\left(\mu + \frac{\mu_t}{N_a}\right)\frac{\partial a_i}{\partial x_j}\right], \quad \text{(B31)}$$

$$\frac{\partial\overline{\rho}\upsilon_{\alpha\beta}}{\partial t} + \frac{\partial\overline{\rho}\upsilon_{\alpha\beta}\widetilde{u}_i}{\partial x_i} = C_{\upsilon1}\mu_t\frac{\partial\widetilde{Y}_\alpha}{\partial x_i}\frac{\partial\widetilde{Y}_\beta}{\partial x_i} - C_{\upsilon2}\overline{\rho}\frac{\sqrt{2k}}{l_d}\upsilon_{\alpha\beta} + \frac{\partial}{\partial x_i}\left[\left(\mu + \frac{\mu_t}{N_\upsilon}\right)\frac{\partial\upsilon_{\alpha\beta}}{\partial x_i}\right]. \quad \text{(B32)}$$

Finally, the model's coefficients have the following values,

$$\begin{array}{ccc} C_{dev} = 16.67 & C_\mu = 0.204 & \mathrm{Pr}_t = 0.060 \\ \mathrm{Sc}_t = 0.060 & C_D = 0.354 & C_{l1} = 0.283 \\ C_{l2t} = -22.96 & C_{l2d} = 0.272 & C_B = 0.857 \\ C_a = 0.339 & C_{\upsilon1} = 46.67 & C_{\upsilon2} = 0.849 \\ N_k = 0.060 & N_{lt} = 0.030 & N_{ld} = 0.030 \\ & N_\upsilon = 0.060. & \end{array} \quad \text{(B33)}$$

The vector a_i is used to model the mass-weighted velocity fluctuation $-\overline{u_i''}$ in the internal energy equation. Additionally, the dissipative term in this equation is modeled as

$$\overline{t'_{ij}\frac{\partial u_i'}{\partial x_j}} = C_D\overline{\rho}\frac{(2k)^{3/2}}{l_d}, \quad \text{(B34)}$$

so as to be consistent with the dissipative term in Eq. (B28). The pressure dilatation term in the internal energy and TKE equations is neglected. A model for b, which represents the density–specific-volume covariance, is still needed—the reader is referred to Refs. [9, 10, 37] for various closures.

[1] S. Davidovits and N. J. Fisch, "Sudden Viscous Dissipation of Compressing Turbulence," Phys. Rev. Lett. **116**, 105004 (2016).

[2] S. I. Braginskii, "Transport processes in plasmas," in *Reviews of Plasma Physics*, Vol. 1 (Consultants Bureau, New York, 1965) p. 205.

[3] C.-T. Wu, J. H. Ferziger, and D. R. Chapman, *Simulation and modeling of homogeneous, compressed turbulence*, Ph.D. thesis, Stanford University (1985).

[4] S. Davidovits and N. J. Fisch, "Compressing turbulence and sudden viscous dissipation with compression-dependent ionization state," Phys. Rev. E **94**, 053206 (2016).

[5] G. Viciconte, B.-J. Gréa, and F. S. Godeferd, "Self-similar regimes of turbulence in weakly coupled plasmas under compression," Phys. Rev. E **97**, 023201

(2018).
[6] A. Campos and B. E. Morgan, "Self-consistent feedback mechanism for the sudden viscous dissipation of finite-mach-number compressing turbulence," Phys. Rev. E **99**, 013107 (2019).
[7] T. R. Dittrich, B. A. Hammel, C. J. Keane, R. McEachern, R. E. Turner, S. W. Haan, and L. J. Suter, "Diagnosis of Pusher-Fuel Mix in Indirectly Driven Nova Implosions," Phys. Rev. Lett. **73**, 2324–2327 (1994).
[8] T. Haxhimali, R. Rudd, W. H. Cabot, and F. R. Graziani, "Shear viscosity for dense plasmas by equilibrium molecular dynamics in asymmetric Yukawa ionic mixtures," Phys. Rev. E **92**, 053110 (2015).
[9] B. E. Morgan, B. J. Olson, W. J. Black, and J. A. McFarland, "Large-eddy simulation and Reynolds-averaged Navier-Stokes modeling of a reacting Rayleigh-Taylor mixing layer in a spherical geometry," Phys. Rev. E **98**, 033111 (2018).
[10] B. E. Morgan, O. Schilling, and T. Hartland, "Two-length-scale turbulence model for self-similar buoyancy-, shock-, and shear-driven mixing," Phys. Rev. E **97**, 013104 (2018).
[11] S. Davidovits and N. J. Fisch, "Modeling turbulent energy behavior and sudden viscous dissipation in compressing plasma turbulence," Phys. Plasmas **24**, 122311 (2017).
[12] A. W. Cook, "Artificial fluid properties for large-eddy simulation of compressible turbulent mixing," Phys. Fluids **19**, 055103 (2007).
[13] C. R. Weber, D. S. Clark, A. W. Cook, D. C. Eder, S. W. Haan, B. A. Hammel, D. E. Hinkel, O. S. Jones, M. M. Marinak, J. L. Milovich, *et al.*, "Three-dimensional hydrodynamics of the deceleration stage in inertial confinement fusion," Phys. Plasmas **22**, 032702 (2015).
[14] C. R. Weber, D. S. Clark, A. W. Cook, L. E. Busby, and H. F. Robey, "Inhibition of turbulence in inertial-confinement-fusion hot spots by viscous dissipation," Phys. Rev. E **89**, 053106 (2014).
[15] C. R. Weber, A. W. Cook, and R. Bonazza, "Growth rate of a shocked mixing layer with known initial perturbations," J. Fluid Mech. **725**, 372–401 (2013).
[16] B. L. Haendler, "Low-density polymer foams for fusion-fuel capsules," in *Energy and Technology Review* (Lawrence Livermore National Laboratory, 1989) pp. 12–20.
[17] L. G. Stanton and M. S. Murillo, "Ionic transport in high-energy-density matter," Phys. Rev. E **93**, 043203 (2016).
[18] M. R. Petersen and D. Livescu, "Forcing for statistically stationary compressible isotropic turbulence," Phys. Fluids **22**, 116101 (2010).
[19] A. Campos and B. Morgan, "The effect of artificial bulk viscosity in simulations of forced compressible turbulence," J. Comput. Phys. **371**, 111–121 (2018).
[20] M. R. Overholt and S. B. Pope, "Direct numerical simulation of a passive scalar with imposed mean gradient in isotropic turbulence," Phys. Fluids **8**, 3128–3148 (1996).
[21] T. Watanabe and T. Gotoh, "Intermittency in passive scalar turbulence under the uniform mean scalar gradient," Phys. Fluids **18**, 058105 (2006).
[22] R. M. Kerr, "High-order derivative correlations and the alignment of small-scale structures in isotropic numerical turbulence," J. Fluid Mech. **153**, 31–58 (1985).
[23] S. Chen and N. Cao, "Anomalous Scaling and Structure Instability in Three-Dimensional Passive Scalar Turbulence," Phys. Rev. Lett. **78**, 3459–3462 (1997).
[24] P. L. Carroll, S. Verma, and G. Blanquart, "A novel forcing technique to simulate turbulent mixing in a decaying scalar field," Phys. Fluids **25**, 095102 (2013).
[25] G. K. Batchelor, "Small-scale variation of convected quantities like temperature in turbulent fluid. Part 1. general discussion and the case of small conductivity," J. Fluid Mech. **5**, 113–133 (1958).
[26] G. A. Blaisdell, G. N. Coleman, and N. N. Mansour, "Rapid distortion theory for compressible homogeneous turbulence under isotropic mean strain," Phys. Fluids **8**, 2692–2705 (1996).
[27] S. B. Pope, *Turbulent Flows* (Cambridge University Press, 2000).
[28] B. E. Launder and B. I. Sharma, "Application of the energy-dissipation model of turbulence to the calculation of flow near a spinning disc," Lett. Heat Mass Transf. **1**, 131–138 (1974).
[29] K.-Y. Chien, "Predicitons of channel and boundary-layer flows with a low-Reynolds-number turbulence model," AIAA J. **20**, 33–38 (1982).
[30] D. C. Wilcox, *Turbulence Modeling for CFD*, 3rd ed. (DCW Industries, Inc., La Cañada, California, 2010).
[31] J. D. Schwarzkopf, D. Livescu, R. A. Gore, R. M. Rauenzahn, and J. R. Ristorcelli, "Application of a second-moment closure model to mixing processses involving multicomponent miscible fluids," J. Turb **12**, 1–35 (2011).
[32] J. D. Schwarzkopf, D. Livescu, J. R. Baltzer, R. A. Gore, and J. R. Ristorcelli, "A two-length scale turbulence model for single-phase multi-fluid mixing," Flow, Turbulence Combust. **96**, 1–43 (2016).
[33] C. G. Speziale and S. Sarkar, "Second-order closure models for supersonic turbulent flows," in *29^{th} Aerospace Sciences Meeting* (Reno, Nevada, 1991).
[34] G. N. Coleman and N. N. Mansour, "Modeling the rapid spherical compression of isotropic turbulence," Phys. Fluids A **3**, 2255–2259 (1991).
[35] S. Sarkar, G. Erlebacher, M. Y. Hussaini, and H. O. Kreiss, "The analysis and modelling of dilatational terms in compressible turbulence," J. Fluid Mech. **227**, 473–493 (1991).
[36] G. Dimonte and R. Tipton, "*K-L* turbulence model for the self-similar growth of the Rayleigh-Taylor

and Richtmyer-Meshkov instabilities," Phys. Fluids **18**, 085101 (2006).
[37] B. E. Morgan and M. E. Wickett, "Three-equation model for the self-similar growth of Rayleigh-Taylor and Richtmyer-Meshkov instabilities," Phys. Rev. E. **91**, 043002 (2015).